Research Article | Vol. 12, No. 4 / 1 Apr 2022 / Optical Materials Express 1480
Optical Materials EXPRESS

Quill-free additive manufacturing of fused silica glass

PAWEL MANIEWSKI,* FREDRIK LAURELL, AND MICHAEL FOKINE

Laser physics group, School of Engineering Science, KTH Royal Institute of Technology, Stockholm, Sweden
pawelma@kth.se

Abstract: Additive manufacturing of high-quality macroscopic fused silica glass structures, with deposition rates of up to 1.2 mm^3/s, is presented. Three co-axial nozzles were used to avoid the so-called quill effect. Homogeneous, crack-free, multilayer, as well as free-standing objects were printed using cluster-free sub-µm powders delivered to a CO_2 laser-induced melt pool. Structures with an overhang of up to 45° were possible to print. Laser post-processing was used to improve the surface roughness and transparency. This system can be suitable for fabrication of advanced optical elements and devices, such as waveguides or fiber preforms.

© 2022 Optica Publishing Group under the terms of the Optica Open Access Publishing Agreement

1. Motivation

Additive manufacturing (AM) commonly known as 3D printing, enables design and fabrication of devices with a complexity that is often unavailable with traditional manufacturing methods [1,2]. Reduced waste and freedom of design are a few examples among multiple benefits of implementing AM in industry. To date AM is typically used for fast prototyping and small-scale production of mechanical components. The palette of available materials in AM is continuously growing. However, technologies for AM of optical materials and components are still limited. In recent years several reports on polymer optical components [3–5] as well as glass objects [6–11] using AM have been published.

Fused silica is a high-performance optical material, recognized for its excellent thermal and chemical stability. However, fabrication and processing of fused silica is typically performed at temperatures exceeding 1500 °C [12]. A suitable method for processing materials with a high melting temperature is laser cladding (LC). Laser cladding is commonly used in metal processing both for component fabrication and repairs, as well as alloying and surface treatment [13,14]. In LC, a high-power laser beam is used to locally melt the surface of a solid substrate. The molten material creates a confined melt pool. Additional material can then be delivered into the melt pool in form of powder, wire or paste [15]. Successful addition of the powder to the substrate is closely related to material properties (viscosity, surface energy) and thermal dynamics of the hot-zone. Under ideal conditions the thermal energy of the melt-pool is sufficient to fully melt and fuse the injected powder, while low enough to avoid extensive material evaporation.

It has been shown that using sub-µm glass powders can mitigate the so-called *shadowing effect*, thereby limiting porosity and inclusions within the build, as reported in Ref. [16,17]. Here, single layer coatings of fully densified fused silica were demonstrated using continuous CO_2 laser irradiation with fumed silica powder, having particle sizes in the range of 0.01 µm to 0.05 µm. The powder was injected into the melt pool using a single, off-axis nozzle. Printing using a single off-axis nozzle resulted in a highly directionally dependent deposition [16]. This effect is commonly referred to as the quill effect [18–20].

Using powder-based LC as-printed objects have a rough, partly sintered and porous surface. One way to post-treat surface defects in printed parts is through mechanical polishing. However, polishing to optical quality is time consuming, adds extra cost to manufactured parts, and is often impossible in case of complex structures. To reduce the need for subtractive processing, e.g., mechanical polishing, and to improve the print quality, laser post-processing can be a very

#448596 https://doi.org/10.1364/OME.448596
Journal © 2022 Received 15 Nov 2021; revised 24 Jan 2022; accepted 4 Feb 2022; published 16 Mar 2022

Optical Materials EXPRESS

interesting approach. Laser scanning can provide highly localized re-melting of structures under controlled conditions [21–24].

In this work we implemented and evaluated quill-free LC using a discrete co-axial print head, featuring integrated shaping gas. Furthermore, we investigated the print quality when using different types of fumed silica powders, having particle surface areas ranging from 85 m^2/g to 700 m^2/g. Fabrication of multi-layer vertical stacks as well as macroscopic, fully densified, free-standing structures were demonstrated with glass deposition rates as high as 1.2 mm^3/s. Additionally, laser post-processing of the printed structures is discussed.

2. Experimental setup and materials

The experimental LC setup was made of four separate parts: (i) CO_2 laser (ULR 50W OEM, Universal Laser Systems) and beam steering optics, (ii) motorized stages for substrate translation in x-y direction and (iii) print head in z-direction, and (iv) a powder feeding system, including vacuum and filtration system for powder evacuation. The optical setup and powder feeder is described in detail in Ref. [16]. All toolpaths were implemented using G-code programming.

In our experiments the Gaussian ($M^2 = 1.2 \pm 0.1$; $\lambda = 10.6$ µm; spot size 1.2 mm; $P_{out} = P_{max}$ ±5%), linearly polarized laser beam was used to locally melt the glass substrate (1 mm thick fused quartz, PlanOptik AG). Fumed silica powder was injected directly onto the normally irradiated substrate. Scanning was initiated simultaneously with the shutter opening and powder feeding. Due to variation in feeding rate and instability of the powder jets (wt/min ±20% [16]) the process was monitored in-situ using a CCD camera (Thorlabs Inc.) in order to compensate for variations in deposition rate.

The printed samples and powders were examined using an optical microscope with back illumination (Nikon Eclipse LV100). To further investigate the cross-sectional quality, samples were diced using a high-speed diamond saw (Disco Corp.) prior to optical inspection. For surface characterization a profilometer (Stylus Profilometer, KLA Tenors P7) was used.

2.1. Discrete co-axial print head with integrated shaping gas

The print head consisted of three identical, symmetrically placed (120° separation) nozzles surrounding the vertically positioned laser beam at an angle of 45° relative to the substrate and the laser beam, as shown in Fig. 1. Each of the 100 mm long nozzles (Ramé-Hart Instrument) were made up of two co-axial stainless-steel tubes having a wall thickness of 0.4 mm with inner diameters of 1.04 mm, and 3 mm, respectively. Both tubes were flush at the exit of the nozzle. Each nozzle was aligned to intersect with the laser beam at the position of the melt zone. Each nozzle was positioned approximately 9 mm away from the melt zone. Glass powder was fed through the inner tube using dry air as a carrier gas (technical dry air, Linde AG). Dry air was also used as shaping gas and controlled using a separate flow regulator. Nozzle details and performance can be found in Ref. [16]. The three nozzles were operating at equal gas flows during printing.

A powder feeder system (Mark XV, Powder Feed Dynamics Inc.) was used to transport powders to the work chamber through an antistatic polyurethane tubing. The powder canister was equipped with an additional heating blanket (Silicone foil heater, IHP AB) to reduce water content and keep the powders dry. Details on the modified powder feeder can be found in Ref. [17].

2.2. Material preparation and characterization

Typical powders used in LC have near-spherical shape with a size in the range of 10 to 200 µm [13–15]. Uniform shape and narrow particle size distribution typically results in high stability in both feeding and deposition rates. However, high purity spherical glass powder in the sub-micron size range is not commonly available in large volumes.

Optical Materials EXPRESS

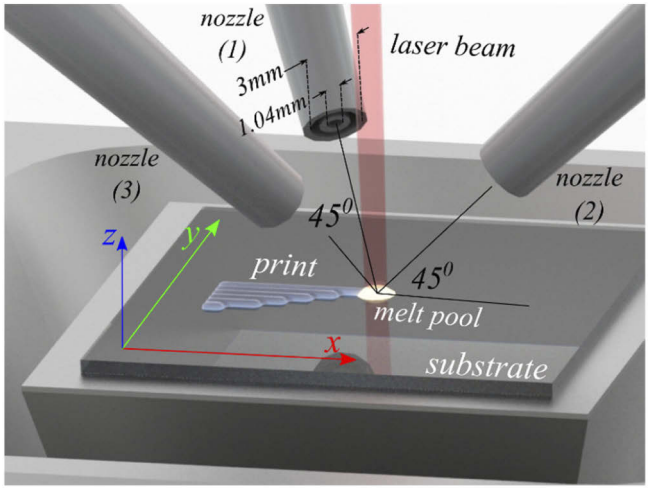

Fig. 1. Schematic of the developed print head consisting of three nozzles with integrated shaping gas symmetrically placed around the laser beam. The powder evacuation system sits below and is not seen in the figure.

Fumed silica typically consists of highly branched particles, where so-called primary particles – nano-sized glass beads – are partially fused together during the production process [25,26]. A common way to describe their structure and shape is by their yield surface area (S.A.). Spherical beads with the same size (≈ 0.05 µm), perfectly packed would correspond to a yield surface area of approx. 33 m^2/g [27]. At the same time a S.A. up to 700 m^2/g is not uncommon for fumed silica, and as such can be beneficial for certain applications [26].

When using fumed silica powders in LC the stability of the powder feeding rate can be affected by (i) humidity, and (ii) the triboelectric effect [28]. If not properly stored fumed silica can adsorb water from the ambient environment causing formation of larger clusters. These clusters will not spontaneously break up even after drying and may hence cause instability in the powder feeding rate. The triboelectric effect causes glass particles to become positively charged after coming in contact with other isolating materials, e.g., plastic storage containers or delivery tubbing [28–30]. Static forces combined with a small mass volume may further hinder powder flowability. When using classic gravitational powder feeders, the triboelectric effect is therefore of major concern.

In our experiments several different types of fumed silica powders were investigated. They were chosen to cover a wide range of S.A., as listed in Table 1.

Table 1. Range of fumed silica powders used in experiments.

Powder reference	P1	P2	P3
S.A. [m^2/g]	85–115	175–225	ca. 700
Supplier	Alfa Aesar	Alfa Aesar	Strem Chemicals
Lot no.	I20W038	R07G095	A0165078

Prior to experiments the powder was loaded into the grounded, stainless steel powder canister. To remove moisture residues a heating blanket (Silicone foil heater, by IHP AB) was mounted on the canister and maintained at a temperature of 100°C. The powder, stored at room temperature prior use, was loaded directly into the heated powder canister. After loading the canister was not fully sealed, allowing natural convection and air exchange. When loading the canister with a volume of 3000 cm^3 of fumed silica, it was experimentally determined that the powder was ready

Optical Materials EXPRESS

to use, i.e., providing a stable powder flow, after 48h of heating. During this time the powder was frequently and thoroughly stirred with a grounded, stainless - steel rod. The feeding rates of each prepared powder were calibrated in the range of 0.4–1.5 g/min [17].

When comparing the print quality using the three different powders, a 12 mm tall free-standing rod was used as a reference structure. During printing, a linearly polarized CO_2 laser beam ($P_{out} = 45$ W) was launched normal to the substrate surface with a powder feed rate of 0.8 g/min. The vertical translation speed was set to 1 mm/s. The printed rods were subsequently removed from the substrate and examined.

2.3. Post-processing of printed structures

Surface engineering of printed structures was performed using a post-processing setup featuring a CO_2 laser (Synrad Firestar 100HS; $\lambda = 10.6$ µm; $M^2 \leq 1.3$; linear polarization)). It was power-stabilized to ±2%. By scanning the surface with the CO_2 laser beam, melting of remaining, partly sintered powder was achieved with a subsequent reduction of surface imperfections. The post-processing layout is shown schematically in Fig. 2(a). The printed rod was first spliced to a 125 µm diameter optical fiber, which was mounted onto a motorized rotational fiber clamp (DC motor, via drive belt). The rod was suspended and aligned vertically by gravity. The fiber clamp was further mounted onto a vertical motorized stage enabling continuous translation of the rod in the axial direction. The focused laser beam could thereby be scanned along the full length of the rotating rod. The spherical lens was mounted on a translation stage allowing fine adjustments of the power density on the rod. During processing the rod could soften and deform due to gravitational force (elongation) and surface tension (contraction). In the extreme case of contraction a glass sphere can be formed [31]. To balance contraction and elongation a counter weight (glass rod of approximately 20 mg ±10 mg) was attached to the end of the rod, as shown in Fig. 2(a). When proper post-processing conditions are met the surface quality was improved, as well as the roundness of the rod. The processing was monitored in-situ using a CCD camera (Thorlabs Inc.) while simultaneously fine-tuning the laser power. A workflow of the post-processing is described in Fig. 2(b).

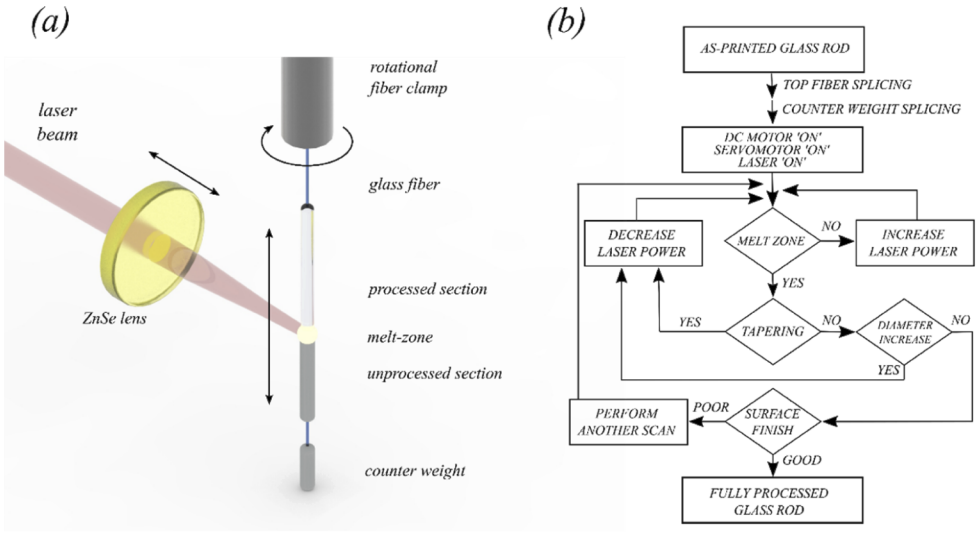

Fig. 2. Schematic (a) of the post-processing setup and (b) the post-processing workflow.

Optical Materials EXPRESS

3. Experimental results

A single, off-axis nozzle provides a simplified approach enabling ease of alignment and is commonly used in LC [15]. To compare the performance and print quality between a single off-axis nozzle and a co-axial print head we printed a vertical wall. The samples presented in this work were printed using the print head discussed in Section 2.1.

3.1. Effect of discrete co-axial print head with an integrated shaping gas flow

As mentioned above the quill effect is the main limitation for printing with a single nozzle and to reduce this effect one would need to print in one direction only [16]. Despite of this there are still angular dependencies in deposition efficiency at the edges of the print. Here, to simulate the conditions occurring during printing using a single off-axis nozzle, two nozzles had been disconnected from the powder feeder line, thus a single powder jet through the nozzle (2) was used (see Fig. 1). This can be seen in Fig. 3(a) where the powder jet is coming from the right, while scanning goes from left to right. After finishing each track, the shutter was closed, and powder injection paused. The print head was then moved back to the starting point and raised with a vertical step equal to the single layer height ($\Delta z = 0.3$ mm). The movement of the print head during printing is indicated by the arrows in Fig. 3(a). Figure 3(b) shows the corresponding structure printed with the co-axial print head. Not suffering from the quill effect printing could be performed continuously without interruption, as indicated by the arrow in the figure. In both cases the print consisted of 20 layers having a thickness of 0.3 mm. The printing speed was set to $v_x = 6.5$ mm/s with a powder feed rate of 0.4 g/min.

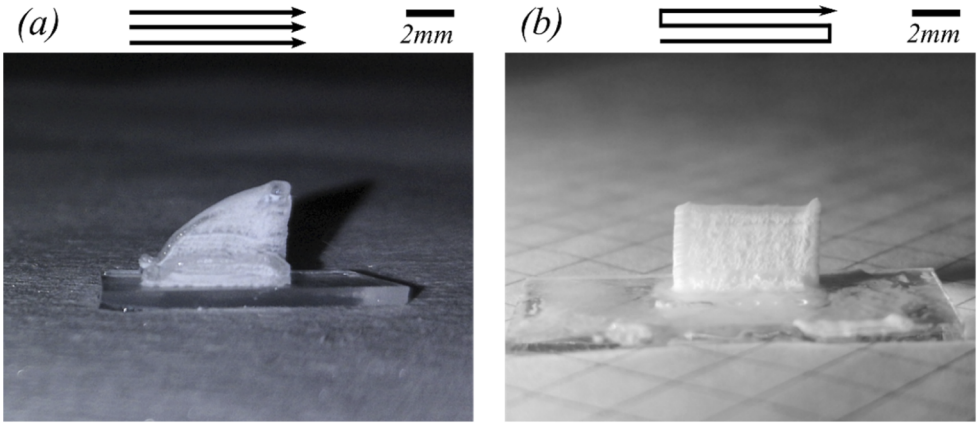

Fig. 3. Objects printed using: (a) the single, off-axis nozzle as in [16] and (b) the symmetric, co-axial print head. The printing directions are indicated by the arrows.

Beside a reduction of total print time of more than 50%, the printed wall using the co-axial print head showed highly symmetric shape. Edge feature seen in Fig. 3(b) is ascribed to stage acceleration and deceleration.

3.2. Printing of free-standing structures

To further evaluate the coaxial print head performance, macroscopic, free-standing structures were printed. A photograph of ongoing printing of a free-standing vertical rod is shown in Fig. 4(a). Structures with a maximum overhang of 45°, defined as the angle between the print and the substrate normal, could be printed without any additional support structures. An example of a free-standing object with several consecutive overhanging sections oriented in different directions is shown in Fig. 4(b). More complicated free-standing prints made up of multiple

Optical Materials EXPRESS

joined sections can be formed, as shown in Fig. 4(c). Here the print consists of four separate sections, schematically shown in Fig. 4(c). This print exemplifies the high control, quality, and flexibility of the developed printing method.

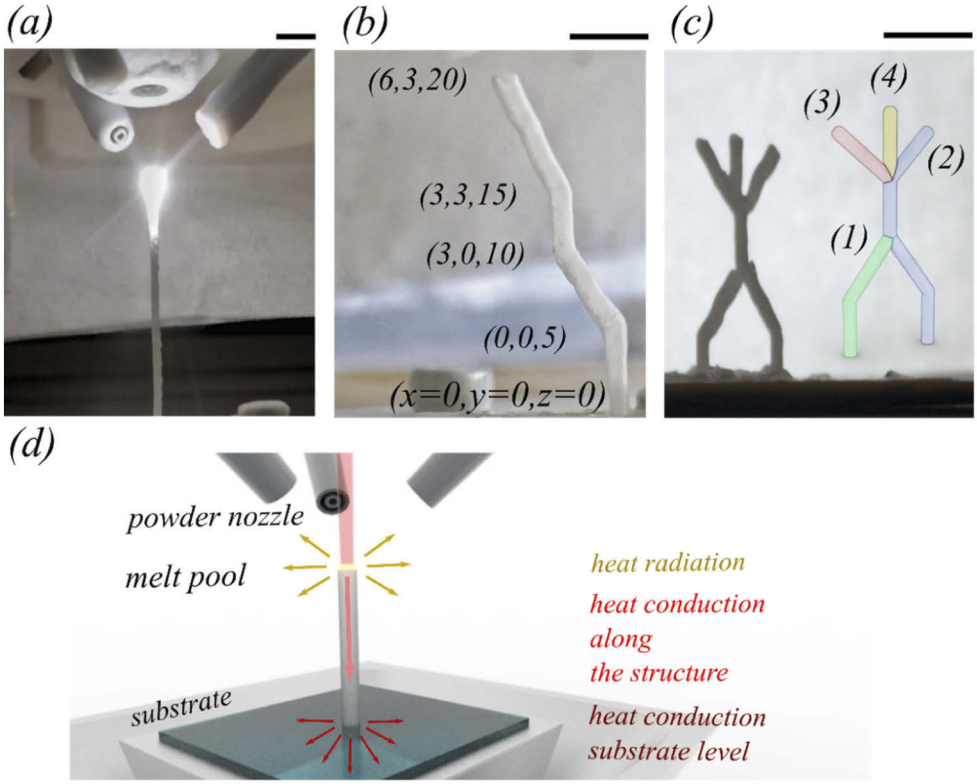

Fig. 4. (a) Photograph taken during printing and (b) example of structure consisting of several overhanging sections. The Cartesian coordinate system indicates the position of each joint. (c) Print of a structure featuring four joined sections. (d) Schematic of the relevant thermal processes taking place during printing. The scale bars correspond to 5 mm.

When printing single layer structures, the size of the melt pool can be larger than the size of the scanning beam due to heat conduction through the substrate [15]. However, when printing free-standing structures, as schematically shown in Fig. 4(d), the melt zone is limited to the size of the print. The lower heat dissipation in this case results in higher melt pool temperature and subsequently higher deposition rates, with up to 1.2 mm^3/s [16].

3.3. Impact of the particle structure

Figure 5 shows microscope images of the three different powders listed in Table 1. They were prepared as described in Section 2.2. The powder, P1, described by the lowest S.A., 85-115 m^2/g, shown in Fig. 5(a), show considerable amounts of large clusters. Powders, P2 and P3, characterized by larger S.A., 175-225 m^2/g and 700 m^2/g, respectively, shown in Fig. 5(b) and Fig. 5(c), show significantly smaller clusters.

Figure 6 shows the rods printed with the three different powders (Fig. 5). They all had, to different degrees, a white, non-transparent appearance as partly sintered powder was attached to the surface. The rod printed using powder P1 was highly porous, irregular in shape and fragile. It was full of defects, such as cracks and voids, and evidently not sufficiently melted along its length. Moreover, during printing using P1 we noticed an unstable powder delivery.

Optical Materials EXPRESS

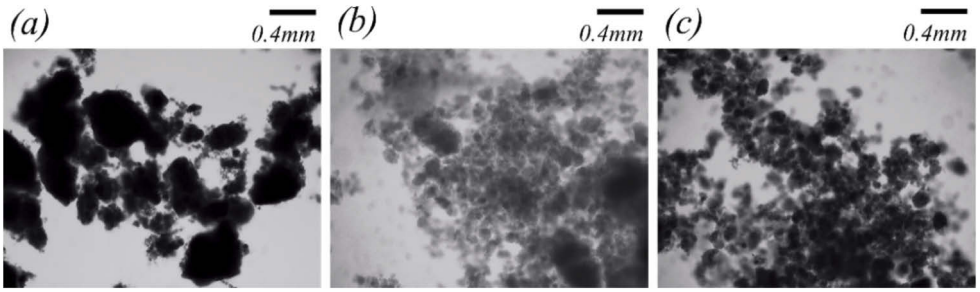

Fig. 5. Images of prepared fumed silica powders extracted directly from powder feeder cannister; (a) P1: S.A. 85-115 m^2/g; (b) P2: S.A. 175-225 m^2/g; (c) P3: S.A.700 m^2/g.

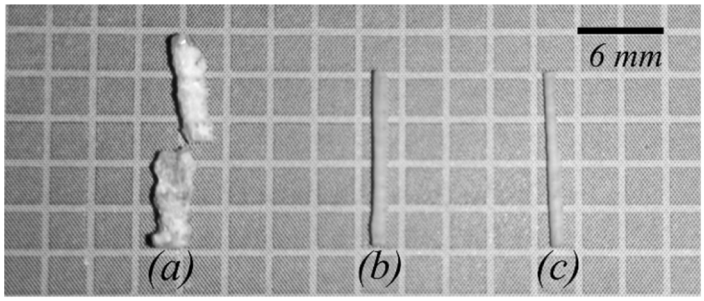

Fig. 6. Image of as-printed rods using powders (a) P1, (b) P2, (c) P3.

The samples printed with powders P2 and P3 were similar in appearance with uniform shape along their full length and without any visible cracks. These rods had diameters of approximately 1.2 mm with slight ovality. Subsequently, the samples were diced in 2 mm long sections and examined using an optical microscope. Typical cross-sections are presented in Fig. 7. The glass at the center of each rods shows fully densified and crack free glass. Voids were found near the edges of the rods with the outer surface containing partly sintered powder. The ovality of the rods was attributed to fluctuations in powder feeding between the three nozzles. We obtained improved feeding stability when using powder P3 which resulted in rods with reduced ovality and less voids in the periphery.

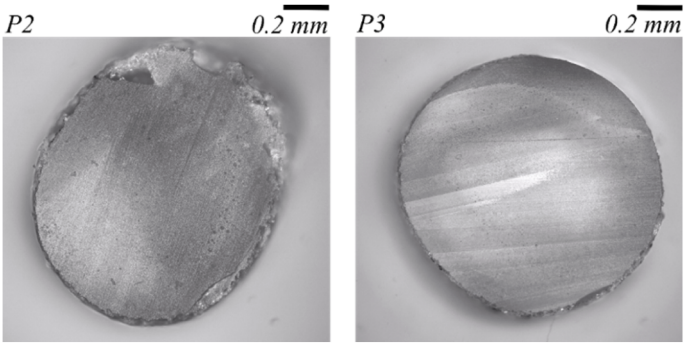

Fig. 7. As-printed fused silica rods using (left) powder P2 and (right) powder P3.

Optical Materials EXPRESS

3.4. Post-processing and surface quality of 3D-printed glass rods

To reduce the number of surface defects and to further homogenize the rods, laser post-processing was used. Due to small differences between printed rods, in-situ process monitoring was used to optimize the result. We found that a relatively fast rotation (40 RPM > v_{rot} > 50 RPM) of the rod combined with a slow linear translation (v_{lin} < 100 µm/s) created the desired surface melting. Side view of post-processed silica rods, with a diameter of approximately 1.1 mm, are shown in Fig. 8(a), with a magnified image shown in Fig. 8(b). Figure 8(c) shows an example of optical imaging through a 4 mm long piece of the same rod. Figure 8(d) shows backlight imaging through crossed polarizers demonstrating that the glass is homogeneous with low built-in stress. Improved surface roughness was shown by profilometer scan along a section of the rod from Fig. 8(a) is shown in Fig. 8(e). The surface roughness of ±0.6 µm was measured. Here, as a comparison, the surface roughness of as-printed rod is shown.

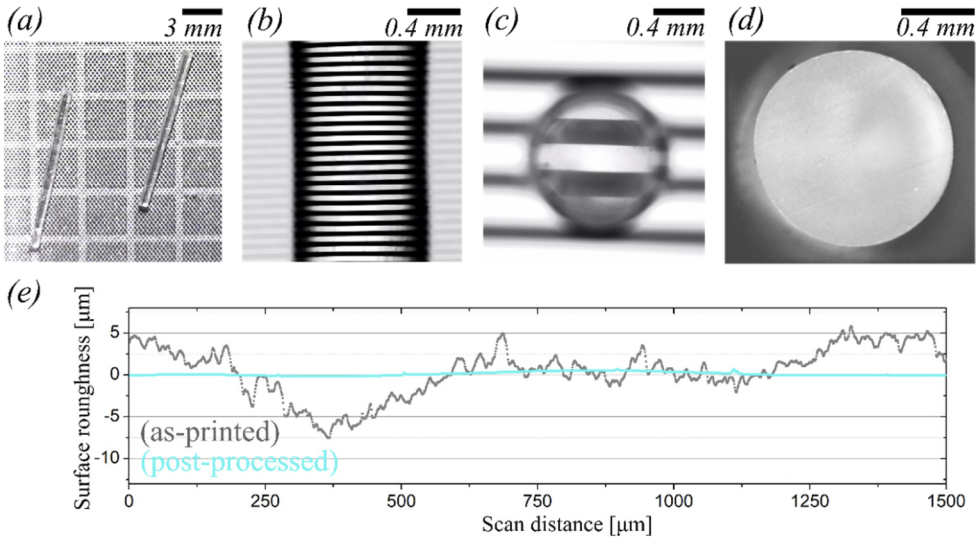

Fig. 8. Photograph (a) of post-processed rods. (b) Microscopic image of a post-processed rod placed on calibration slide with a line spacing of 100 µm and (c) top view through a 4 mm long post-processed rod with back illumination placed on a slide with line spacing of 0.4 mm, and (d) the same rod seen through crossed polarizers. The end-faces of the rod seen in (c) and (d) were cut using a diamond saw, i.e., unpolished. (e) Typical surface roughness of a rod, before and after post-processing.

4. Discussion

We have developed a co-axial print head for LC and compared it to a single off-axis layout for printing of fused silica glass. With our new setup a symmetric shape of the test sample was achieved when printing was performed in two opposite scanning directions, showing elimination of the quill-effect, increased deposition rates and improved homogeneity as visualized through crossed polarizers (Fig. 8(d)). Deposition rates of up to 1.2 mm^3/s were achieved, nearly three times as high as in previous work [16]. The test sample, a crack free, vertical wall was printed, consisting of 20 layers placed on top of each other (8.5 mm long, 1.1 mm wide and 5.6 mm tall). The width of the print was equal to the width of a single deposition track, within the typical 3D printer's tolerance (± 0.2 mm). Structural features appearing on each end of the print were due to stage acceleration and deceleration.

Optical Materials EXPRESS

The new print head enabled printing of true 3D structures by translation of the melt-pool in three dimensions. To the best of our knowledge, fabrication of macroscopic free-standing objects has not been demonstrated before using direct glass powder deposition. The maximum print height was limited by the stroke range of the setup, which was 40 mm in this work. Free-standing macroscopic objects, with an overhang of up to 45° were successfully printed. By increasing the angle further, the melt zone is reduced in size, resulting in possible formation of a secondary hot zone on structures below, as seen in Fig. 9. This secondary hot zone can trap and sinter ambient powder, which can lead to undesirable dimensional changes of the printed object. A simple way to mitigate this effect is to use a lens with high numerical aperture. However, it is important that the lens has a sufficiently long working distance to avoid getting too close to the melt pool, which could lead to contamination and overheating of the lens. In our experiments the diameter of the laser induced hot zone was 1.2 mm, slightly larger than the diameter of the powder jets reaching the melt pool. However, the print size can easily be changed by adjusting the laser spot size according to the specific application.

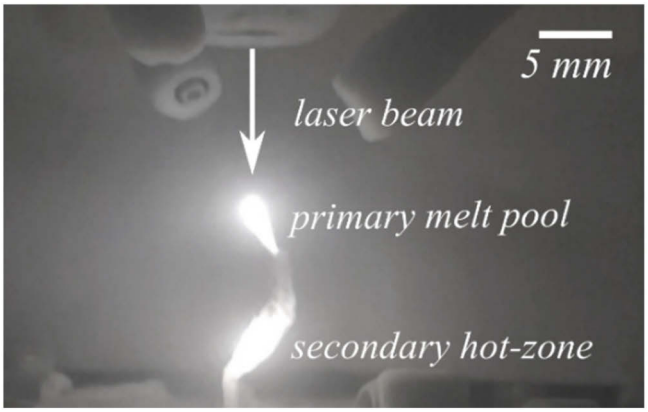

Fig. 9. Photograph of ongoing printing of large overhang showing secondary hot zone.

When comparing three types of fumed silica with different S.A., as specified in Table 1, the powders with high S.A. gave the best results. The powder with the lowest S.A., (P1), contained large clusters, as seen in Fig. 5(a) that caused powder feeding fluctuations and nozzle clogging. Additionally, the clusters led to unwanted shadowing effects with subsequent incomplete melting of the powder, resulting in gaps and not fully melted areas within the printed structure. The reasons for these large clusters to appear are unknown. Stable powder feeding and successful printing was obtained when using fumed silica with larger S.A. (200 m^2/g and 700 m^2/g).

5. Conclusions

In this work additive manufacturing of high-quality macroscopic fused silica glass structures was performed using powder-based laser cladding. A CO_2 laser was used to create the melt pool. To reduce the quill effect a print head consisting of three co-axial nozzles was developed. Printing was achieved by translation of the melt pool, in three dimensions, while simultaneously injecting the silica powder.

The best results were achieved when using a high-surface area, sub-µm powder with low amount of clustering. Homogeneous, crack-free objects were obtained with deposition rates of up to 1.2 mm^3/s. Printing free-standing structures with an overhang of up to 45°, consisting of several intersecting sections was demonstrated without use of support structures. With additional

Optical Materials EXPRESS

laser post-processing the surface finish and transparency of the prints was further improved. Surface roughness of up to ±0.6 µm was measured on post-processed test samples.

Attractive features of the developed method include the possibility to adjust the spot size to attain desired dimensions of the print, as well as the possibility to change the powder composition during printing to obtain heterogeneous objects. This would enable fabrication of advanced, tailored optical elements and devices, such as waveguides or fiber preforms.

Funding. Knut och Alice Wallenbergs Stiftelse (2016.0104); Stiftelsen för Strategisk Forskning (GMT14-0071, RMA150135).

Acknowledgments. We acknowledge the Swedish Foundation for Strategic Research and the K.A. Wallenberg foundation for financial support, and Korbinian Mühlberger for access to the CO_2 laser system used for post-processing, and Laura Barett for help with the profilometer measurements.

Disclosures. The authors declare no conflicts of interest.

Data availability. Data underlying the results presented in this paper are not publicly available at this time but may be obtained from the authors upon reasonable request.

References

1. D. W. Rosen, B. Stucker, and I. Gibson, *Additive Manufacturing Technologies: 3D Printing, Rapid Prototyping, and Direct Digital Manufacturing* (Springer, 2010).
2. T. D. Ngo, A. Kashani, G. Imbalzano, K. T. Q. Nguyen, and D. Hui, "Additive manufacturing (3D printing): a review of materials, methods, applications and challenges," Composites, Part B **143**, 172–196 (2018).
3. K. Cook, J. Canning, S. Leon-Saval, Z. Reid, M. Hossain, J. Comatti, Y. Luo, and G. Peng, "Air-structured optical fiber drawn from a 3D-printed preform," Opt. Lett. **40**(17), 3966–3969 (2015).
4. B. Assefa, M. Pekkarinen, H. Partanen, J. Biskop, J. Turunen, and J. Saarinen, "Imaging-quality 3D-printed centimeter-scale lens," Opt. Express **27**(9), 12630–12637 (2019).
5. E. N. Udofia and W. Zhou, "3D printed optics with a soft and stretchable optical material," Addit. Manuf. **31**, 100912 (2020).
6. J. Klein, M. Stern, G. Franchin, M. Kayser, C. Inamura, and S. Dave, "Additive manufacturing of optically transparent glass," 3D Print. Additive Manuf. **2**(3), 92–105 (2015).
7. F. Kotz, K. Arnold, W. Bauer, D. Schild, N. Keller, K. Sachsenheimer, T. M. Nargang, C. Richter, D. Helmer, and B. E. Rapp, "Three-dimensional printing of transparent fused silica glass," Nature **544**(7650), 337–339 (2017).
8. R. Dylla-Spears, T. D. Yee, K. Sasan, D. T. Nguyen, N. A. Dudukovic, J. M. Ortega, M. A. Johnson, O. D. Herrera, F. J. Ryerson, and L. L. Wong, "3D printed gradient index glass optics," Sci. Adv. **6**(47), eabc7429 (2020).
9. K. Rettschlag, A. Hohnholz, P. Jäschke, D. Kracht, S. Kaierle, and R. Lachmayer, "Laser glass deposition of spheres for printing micro lenses," Proc. CIRP **94**, 276–280 (2020).
10. D. G. Moore, L. Barbera, K. Masania, and A. R. Studart, "Three-dimensional printing of multicomponent glasses using phase-separating resins," Nat. Mater. **19**(2), 212–217 (2020).
11. T. Grabe, M. Lammers, S. Wang, X. Wang, K. Rettschlag, K. Sleiman, A. Barroi, T. Biermann, A. Ziebehl, J. Röttger, P.-P. Ley, A. Wolf, P. Jaeschke, J. Hermsdorf, S. Kaierle, H. Ahlers, and R. Lachmayer, "Additive manufacturing of fused silica using coaxial laser glass deposition: experiment, simulation, and discussion," Proc. SPIE **11677**, 116770Z (2021).
12. M. Yamane and Y. Asahara, *Glasses for Photonics* (Cambridge University, 2000), Chap. 1.
13. X. Zhang, S. Pfeiffer, P. Rutkowski, M. Makowska, D. Kata, J. Yang, and T. Graule, "Laser cladding of manganese oxide doped aluminum oxide granules on titanium alloy for biomedical applications," Appl. Surf. Sci. **520**, 146304 (2020).
14. W. Yuan, R. Li, Z. Chen, J. Gu, and Y. Tian, "A comparative study on microstructure and properties of traditional laser cladding and high-speed laser cladding of Ni45 alloy coatings," Surf. Coat. Technol. **405**, 126582 (2021).
15. E. Toyserkani, A. Khajepour, and S. F. Corbin, *Laser Cladding* (CRC, 2005).
16. P. Maniewski, F. Laurell, and M. Fokine, "Laser cladding of transparent fused silica glass using sub-micron powder," Opt. Mater. Express **11**(9), 3056–3070 (2021).
17. P. Maniewski, F. Laurell, and M. Fokine, "Reduction of shadowing effect during laser cladding of fused silica glass using sub-micron powders," Proc. SPIE **11677**, 1167711 (2021).
18. K. Sugioka and Y. Cheng, "Femtosecond laser three-dimensional micro- and nanofabrication," Appl. Phys. Rev. **1**(4), 041303 (2014).
19. J. Guan, X. Liu, and M. J. Booth, "Ultrafast laser writing quill effect in low loss waveguide fabrication regime," Opt. Express **26**(23), 30716–30723 (2018).
20. P. G. Kazansky, W. Yang, and E. Bricchi, ""Quill" writing with ultrashort light pulses in transparent materials," Appl. Phys. Lett. **90**(15), 151120 (2007).
21. P. Cormont, P. Combis, L. Gallais, C. Hecquet, L. Lamaignère, and J. L. Rullier, "Removal of scratches on fused silica optics by using a CO_2 laser," Opt. Express **21**(23), 28272–28289 (2013).

Optical Materials EXPRESS

22. M. J. Matthews, S. T. Yang, N. Shen, S. Elhadj, R. N. Raman, G. Guss, I. L. Bass, M. C. Nostrand, and P. J. Wegner, "Micro-shaping, polishing, and damage repair of fused silica surfaces using focused infrared laser beams," Adv. Eng. Mater. **17**(3), 247–252 (2015).
23. E. Mendez, K. M. Nowak, H. J. Baker, F. J. Villarreal, and D. R. Hall, "Localized CO_2 laser damage repair of fused silica optics," Appl. Opt. **45**(21), 5358–5367 (2006).
24. S. Heidrich, E. Willenborg, C. Weingarten, and A. Temmler, "Laser polishing and laser form correction of fused silica optics," Materialwiss. Werkstofftech. **46**(7), 668–674 (2015).
25. J. Liu, Y. E. Kutsovsky, and G. P. Fotou, "Process for the production of fumed silica," U.S. patent US 2007/0253884 A1 (2007).
26. H. Barthel, M. Heinemann, M. Stintz, and B. Wessely, "Particle sizes of fumed silica," Part. Part. Syst. Charact. **16**(4), 169–176 (1999).
27. W. Dai, J. Reimann, D. Hanaor, C. Ferrero, and Y. Gan, "Modes of wall induced granular crystallisation in vibrational packing," Granular Matter **21**(2), 26 (2019).
28. D. Tucholski and G. M. Colver, "Charging of glass powder in a circulating fluidized bed," *IEEE Industry Applications Conference* **3**, 1906–1912 (1998).
29. U. Lesprit, T. Paillat, N. Zouzou, A. Paquier, and M. Yonger, "Triboelectric charging of a glass bead impacting against polymers: Influence of mechanical properties," J. Electrost. **107**, 103474 (2020).
30. D. J. Lacks and R. Mohan Sankaran, "Contact electrification of insulating materials," J. Phys. D: Appl. Phys. **44**(45), 453001 (2011).
31. C. Harvey, K. Mühlberger, and M. Fokine, "Non-contact Interferometric Technique for Fabrication of Silica Microspheres with Improved Ellipticity," in Optical Sensors and Sensing Congress, OSA Technical Digest (Optical Society of America, 2020), paper SM1B.7.